J. Fluid Mech. (2014), *vol.* 747, *pp.* 44–72. © Cambridge University Press 2014
doi:10.1017/jfm.2014.155

Disturbance energy growth in core–annular flow

A. Orazzo, G. Coppola† and L. de Luca

Dipartimento di Ingegneria Industriale, Università degli studi di Napoli 'Federico II', Naples, 80125, Italy

(Received 2 August 2013; revised 31 January 2014; accepted 17 March 2014;
first published online 10 April 2014)

The linear stability of the horizontal pipe flow of an equal density oil–water mixture, arranged as a *core–annular flow* (CAF), is here reconsidered from the point of view of non-modal analysis in order to assess the effects of non-normality of the linearized Navier–Stokes operator on the transient evolution of small disturbances. The aim of this investigation is to give insight into physical situations in which poor agreement occurs between the predictions of linear modal theory and classical experiments. The results exhibit high transient amplifications of the energy of three-dimensional perturbations and, in analogy with single-fluid pipe flow, the largest amplifications arise for non-axisymmetric disturbances of vanishing axial wavenumber. Energy analysis shows that the mechanisms leading to these transient phenomena mostly occur in the annulus, occupied by the less viscous fluid. Consequently, higher values of energy amplifications are obtained by increasing the gap between the core and the pipe wall and the annular Reynolds number. It is argued that these linear transient mechanisms of disturbance amplification play a key role in explaining the transition to turbulence of CAF.

Key words: core–annular flow, instability, multiphase and particle-laden flows

1. Introduction

The stationary concentric flow of two immiscible fluids in a pipe, commonly referred to as core–annular flow (CAF), is quite a classical configuration in fluid dynamics. Apart from the purely academic interest, this class of simple flows has been extensively studied in the past, both experimentally and theoretically, because of the strong tendency of two immiscible fluid systems flowing in a pipe to arrange themselves so that the low-viscosity fluid is in the annular region of high shear. The technological applications of this type of spontaneous arrangement, usually related to the lubricated transport of highly viscous fluids, has driven the research on CAF mainly with respect to the stability of the ideal concentric configuration. In fact, the major beneficial effect of the introduction of less viscous fluid (say water) in a pipe transporting a viscous fluid (say oil) is the reduction of the pressure gradient along the pipeline and thus of the power necessary to pump a given quantity of the viscous fluid. This beneficial effect is partially or completely lost when the ideal configuration breaks up, and the conditions under which this transition occurs have been the subject of much research in the past (Charles, Govier & Hodgson 1961; Charles & Redberger 1962; MacLean 1973; Oliemans & Ooms 1986).

The literature on the stability of CAF configurations is quite large. The studies of interest for the present investigation pertain to the so-called 'perfect' core–annular flow

† Email address for correspondence: gcoppola@unina.it

https://doi.org/10.1017/jfm.2014.155 Published online by Cambridge University Press

(PCAF), which is the highly symmetric configuration established in horizontal pipes when the two fluids have the same density, and therefore gravity effects are nullified. For such simplified configurations classical linear stability analysis reduces, by means of a normal mode position, to eigenvalue problems for ordinary differential equations in the radial direction. Early studies on the linear stability of PCAF were conducted by Hickox (1971), Joseph, Renardy & Renardy (1985), Hu & Joseph (1989), Preziosi, Chen & Joseph (1989) and many others. A comprehensive review on the subject up to the early 1990s can be found in Joseph & Renardy (1991). These stability analyses showed that the PCAF configuration is typically stable only when the more viscous fluid is located in the core and occupies most of the pipe, so the volume ratio between the two fluids is a crucial factor. In fact, even in the case of a thin lubricating layer, the stability depends on the flow conditions, such as, for example, when the flow is slow and capillary instability is induced by interfacial tension. Inertia has a stabilizing effect (Chen & Joseph 1991) and the capillary instability can be completely stabilized by increasing the Reynolds number (Preziosi *et al.* 1989). In general, the parameter range for which CAF is stable is quite small.

A series of classical experiments on CAF of two fluids having the same density is reported in the paper by Charles *et al.* (1961) (hereafter referred to as CGH). As shown in figures 3–5 of CGH (also reported in Preziosi *et al.* 1989, hereafter PCJ, and Hu & Joseph 1989), the instability of the PCAF configuration typically evolves into different types of flow patterns which can be roughly divided into two classes: in some situations the interface breaks up into regular bubbles or slugs, in others the flow is characterized by emulsifications or water drops in oil. The linear modal stability analysis, while being successful in predicting flow transition typically evolving in regular slugs or bubbles, does not completely explain the transition to particular flow patterns falling in the second class. The modal analysis performed by PCJ, and conducted by considering the experimental conditions of CGH, explains the first kind of flow pattern as the result of a long-wave instability due to surface tension and is able to correlate the sizes of the bubbles and slugs (produced as the final stage of the instability) with the wavelength of the fastest growing wave. The second type of CAF instability, visible in experiments 1, 5, 6, 9 and 10 of CGH, is partially correlated with strong short-wave instabilities and partially remains unexplained. In commenting on their results, PCJ say that 'The smaller water bubbles shown in Experiments 6 and 9 and the oil bubbles in Experiment 10 are unexplained by this analysis. They could arise as a reaction to turbulence in the water, or as kind of secondary instability of slugs.' However, the mechanisms by which these effects arise remain undetermined.

Linear stability analysis is a wider concept than modal stability analysis. A recurrent theme in recent studies on linear hydrodynamic instability of shear flows is the concept of non-modal growth of energy, which identifies a linear mechanism of transient amplification of disturbances in asymptotically stable systems. Transient growth is a mathematical phenomenon due to the non-normality of the governing linear operator, the implications of which for hydrodynamic stability have been quite firmly estabilished in recent years (e.g. Trefethen *et al.* 1993 and Schmid 2007). The non-modal theory has been extensively used in the recent past in order to explain the experimentally observed transition to turbulence at subcritical Reynolds numbers for a wide class of canonical flows. In light of the recent results on transient growth in CAF reported in the paper by Coppola, Orazzo & de Luca (2012), in this paper we consider the linear non-modal stability analysis for ranges of parameters matching the conditions of classical and more recent experiments to ascertain whether non-modal mechanisms are relevant in explaining the partial failure of classical modal analysis.

https://doi.org/10.1017/jfm.2014.155 Published online by Cambridge University Press

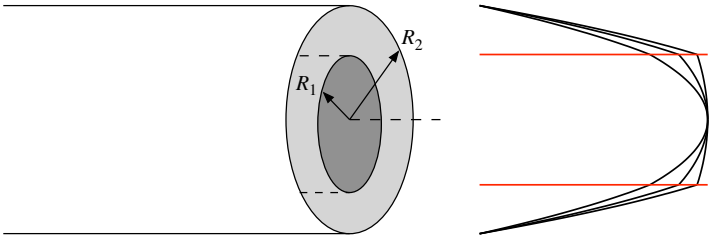


FIGURE 1. (Colour online) The geometry of core–annular flow and velocity profiles referred to different values of m.

2. Governing equations and numerical method

2.1. *Linearized equations and transient growth*

Two liquids flowing in a cylindrical pipe of radius R_2 and infinite length are considered. The interface equation between the two liquids is given by $r = R(\theta, x, t)$, where t is time, (r, θ, x) are the cylindrical polar coordinates and the corresponding components of velocity are denoted by $\boldsymbol{U} = (U, V, W)$. In the steady unperturbed configuration the region $0 \leqslant r \leqslant R_1$, where R_1 is a constant radius determined by the prescribed volumes of the two liquids, is occupied by the first liquid of viscosity and density μ_1 and ρ_1 respectively, while the second liquid (whose properties are denoted by μ_2 and ρ_2) is located in the annular region $R_1 \leqslant r \leqslant R_2$.

The base flow is parallel and is modeled as a Hagen–Poiseuille (HP) flow, driven by a prescribed pressure gradient, the velocity field being $\overline{\boldsymbol{U}} = (0, 0, \overline{W}(r))$. By scaling lengths with R_1 and velocity with the centreline velocity $\overline{W}(0) = W_0$, we obtain the following dimensionless velocity $\overline{W}(r)$ (note that for the sake of simplicity the symbol r will denote hereafter the dimensionless radial coordinate):

$$\overline{W}(r) = \begin{cases} 1 - mr^2/(a^2 + m - 1), & 0 \leqslant r \leqslant 1, \\ (a^2 - r^2)/(a^2 + m - 1), & 1 \leqslant r \leqslant a, \end{cases} \tag{2.1}$$

where $m = \mu_2/\mu_1$ is the viscosity ratio and $a = R_2/R_1$ is the dimensionless outer radius of the pipe. Figure 1 shows the base flow for different values of m starting from the classic parabolic HP flow for $m = 1$.

In order to perform the linear stability analysis, we classically perturb the base flow, so that the total velocity components, pressure and interface position are

$$\boldsymbol{U} = (u, v, \overline{W} + w), \quad P = \overline{P} + p, \quad R = 1 + \delta(\theta, x, t), \tag{2.2a–c}$$

where capital letters denote (total) perturbed quantities, lower-case letters denote infinitesimal disturbances and the bar refers to the base flow. Here, δ is the interface disturbance.

Fourier decomposition in the azimuthal and axial directions, and the temporal normal mode position, lead to the following expressions for disturbance quantities:

$$\left.\begin{aligned} [u, v, w, p](r, \theta, x, t) = [\mathrm{i}\tilde{u}, \tilde{v}, \tilde{w}, \tilde{p}](r)\mathrm{e}^{\mathrm{i}(n\theta + kx - \omega t)}, \\ \delta(\theta, x, t) = \tilde{\delta}\mathrm{e}^{\mathrm{i}(n\theta + kx - \omega t)}, \end{aligned}\right\} \tag{2.3}$$

where $n \in \mathbb{Z}$ and $k \in \mathbb{R}$ are the azimuthal and axial wavenumbers and ω is a complex number representing the temporal frequency. The real and imaginary parts of ω are

https://doi.org/10.1017/jfm.2014.155 Published online by Cambridge University Press

respectively ω_r and ω_i and the amplitude functions (eigenfunctions) are denoted by the symbol '$\sim$'. Using these perturbation quantities the linearized Navier–Stokes equations are reorganized into the following generalized eigenvalue problem:

$$-\mathrm{i}\omega\mathscr{M}\tilde{\boldsymbol{q}} = \mathscr{A}\tilde{\boldsymbol{q}}, \tag{2.4}$$

where $\tilde{\boldsymbol{q}}$ contains core and annular velocity components, pressure and the displacement disturbance of the interface. Here, $\mathscr{M}$ is the unsteady operator and $\mathscr{A}$ is the convection–diffusion operator.

The linearized equations are closed by specifying boundary and interface conditions. The velocity has to satisfy homogeneous boundary conditions at the pipe wall and regularity conditions at $r = 0$ in order to be continuous and single-valued (see Khorrami, Malik & Ash 1989 and Ash & Khorrami 1995). The kinematic condition and the continuity of both velocity and stress tensor components are imposed at the interface. The full expressions for the entries of $\mathscr{M}$ and $\mathscr{A}$ are given in appendix A, together with the expressions for interface and axis conditions. Further details on the derivation of the linearized problem (2.4) and on the boundary conditions are contained in PCJ and in the paper by Coppola *et al.* (2012).

The problem is characterized by five independent dimensionless parameters: m, a, ζ, J, Re_1. Here, J is a parameter relating the effects of surface tension, inertia and viscosity, $J = (TR_1)/(\rho_1\nu_1^2)$, in which T is the surface tension coefficient, Re_1 is the core Reynolds number, $Re_1 = (W_0R_1\rho_1)/\mu_1$, and ζ is the density ratio, $\zeta = \rho_2/\rho_1$. In some circumstances a different choice of the set of independent parameters could be more advantageous. As observed by PCJ, for example, from the experimental viewpoint the parameter $J^* = aJ$ is usually preferable, since it remains constant on varying the superficial velocities (i.e. volumetric flow rates per unit pipe section) of the phases. An annular Reynolds number Re_2 is also usually employed, which is still based on the centreline velocity W_0 and the core radius R_1, but considers the annular fluid's kinematic viscosity. This definition naturally arises in the equations of motion when one scales lengths with R_1, velocities with the centreline velocity W_0 and time with R_1/W_0. A different definition for the annular Reynolds number would be based on the velocity at the interface and the difference between the interface and pipe radii, $Re_2^* = (W(R_1)(R_2 - R_1)\rho_2)/\mu_2$. The relation between Re_2 and Re_2^* is given by

$$Re_2^* = Re_2\left(\frac{a(a-1)(a^2-1)}{a^2+m-1}\right). \tag{2.5}$$

In what follows we will assume that the two fluids have the same density ($\zeta = 1$), thus the Reynolds numbers of the core and of the annulus are related by $Re_1/Re_2 = m$.

To perform non-modal instability analysis the starting point is to rewrite the linearized governing equations as the following initial-value problem:

$$\frac{\partial\hat{\boldsymbol{q}}}{\partial t} = \mathscr{L}\hat{\boldsymbol{q}}, \tag{2.6}$$

where $\mathscr{L}$ is the linearized operator, symbolically written as $\mathscr{L} = \mathscr{M}^{-1}\mathscr{A}$. The vector $\hat{\boldsymbol{q}}$ contains core and annular Fourier components of disturbance flow variables and disturbance displacement of the interface.

As a measure of the disturbance energy we define the energy norm,

$$E(t) \;=\; \|\hat{\boldsymbol{q}}\|_E^2 = \frac{1}{2}\int_0^1 (|\hat{u}_1|^2 + |\hat{v}_1|^2 + |\hat{w}_1|^2) r\mathrm{d}r$$

https://doi.org/10.1017/jfm.2014.155 Published online by Cambridge University Press

$$+\frac{1}{2}\int_1^a (|\hat{u}_2|^2+|\hat{v}_2|^2+|\hat{w}_2|^2)r\mathrm{d}r+\frac{1}{2}\frac{J}{Re_1^2}(n^2+k^2)|\hat{\delta}|^2, \tag{2.7}$$

where the two integrals represent the kinetic energy of the disturbance in the core and in the annulus. The last term in (2.7) accounts for the contribution of interfacial capillary energy and is proportional to the surface increment of the perturbed interface with respect to the cylindrical surface having the same mean radius. Note that the mean radius of the perturbed interface is in general different from the unperturbed interface radius, since the perturbation of the surface has to be carried out at constant volume. As the difference between these two radii is of second order in the amplitude of the disturbance, it is not necessary to distinguish between them in the derivation of the linearized interface conditions. The surface energy variation, on the other hand, is different in the two cases since, for example, it can be negative for axisymmetric disturbances with long wavelength ($k < 1$) when measured with reference to the unperturbed configuration.

Using this norm the transient growth function of an initial disturbance, $G(t)$, is thus defined as

$$G(t)=\|\mathrm{e}^{t\mathscr{L}}\|_E^2=\max_{\hat{\boldsymbol{q}}(0)\neq 0}\frac{\|\hat{\boldsymbol{q}}(t)\|_E^2}{\|\hat{\boldsymbol{q}}(0)\|_E^2}. \tag{2.8}$$

This gain function $G(t)$ gives the maximum energy amplification of a perturbation optimized over all possible initial conditions $\hat{\boldsymbol{q}}(0)$; hence, it is the envelope of the energy evolution of all initial conditions with unit norm.

2.2. *Numerical treatment*

The generalized eigenvalue problem (2.4) has been discretized along the radial direction separately for the fluid in the core and in the annulus by employing a standard Chebyshev collocation method. For both fluids the finite domain is mapped to the interval $[-1, 1]$ via a linear transformation. Boundary conditions on the pipe wall and axis are enforced by replacing rows and interface conditions are treated as boundary conditions for each fluid.

The spectral discretization employed for the computation of eigenvalues has been used also to compute the transient growth function $G(t)$ by means of an eigenmode expansion method (Schmid & Henningson 2001). The energy norm is calculated by transforming it into a standard 2-norm by employing a singular value decomposition (SVD) of the matrix of inner products between the eigenvectors, which was found to be numerically more stable than the classical Cholesky decomposition.

In order to implement this procedure a certain number of eigenvalue–eigenvector pairs has to be determined. We performed an accurate convergence check for each pair employed in the computation of $G(t)$. It has been previously reported that in the two-fluid flow system the computation of $G(t)$, obtained by superimposing a finite number of eigenfunctions, can suffer from non-convergent behaviour as the number of eigenfunctions is increased (see Malik & Hooper 2007). This behaviour is present in cases in which surface tension is not considered and, in fact, it is due to the omission of an interfacial energy term in the definition of $G(t)$. Since in this paper J is non-zero, the interfacial energy term is present and the convergence of $G(t)$ is always reached with a number of eigenfunctions that is typically smaller than 80.

In selected configurations the growth function $G(t)$ at fixed values of the parameters has been computed. In other cases a parametric study of the maximum value G_{MAX}, attained by $G(t)$ over time at different values of the Reynolds and axial wavenumbers,

https://doi.org/10.1017/jfm.2014.155 Published online by Cambridge University Press

has been performed. For such computations the value of G_{MAX} is calculated with high accuracy by employing a golden-section search on $G(t)$. The so-called *optimal perturbations*, i.e. the initial conditions attaining the maximum value of energy among all the possible initial conditions with unit norm, are also calculated via an SVD procedure of the transformed matrix exponential of (2.8).

Two different versions of the code have been used for the analysis presented here: a three-equation version, obtained by eliminating pressure from the linearized Navier–Stokes equations, and a four-equation version, employed to have better accuracy for $k \to 0$.

A convergence study for these codes, already used by the authors in Coppola *et al.* (2012) (see also Coppola & Semeraro 2011 for a different application), has shown that a total number of collocation points $120 \leqslant N \leqslant 170$ has to be adopted. An *ad hoc* procedure has been developed in order to split N between the two fluids depending on the values of a and m.

2.3. *Code validation*

The pseudospectral code has been validated against several modal and non-modal calculations reported in the literature. First of all, we verified that, by setting $J = 0$ and $m = \zeta = 1$, our code completely reproduces the modal and non-modal results for the classical HP flow, apart from a neutral eigenmode related to the interface variable. In this section we report some representative comparisons of our results with analogous calculations already documented in previous work for the two-fluid case. In table 1 the convergence history of our pseudospectral code is reported, together with the analogous results presented in Hu & Joseph (1989), which were computed with a finite element code. The c_i are the most unstable eigenvalues (in our notation $c = \omega/k$) for three cases selected in Hu & Joseph (1989), which are expressed by the following sets of values for the parameters $(J, a, m, \zeta, n, k, Re_1)$. c_1: (900, 1.11, 0.05, 1, 0, 4.5, 450); c_2: (0, 1.43, 0.5, 1, 0, 7, 26.45); c_3: (0, 1.43, 0.5, 1, 5, 7, 26.45). N_1 and N_2 are the numbers of nodes (or elements) in the core and annular phase respectively. The table shows that a total number of collocation points of approximately 20 in each phase is sufficient to assure the convergence up to five figures for both the real and the imaginary parts of the most unstable eigenfrequency. In order to achieve the same accuracy in the whole part of the spectrum employed for the calculation of the growth function, this number has to be increased to a value typically between 50 and 80.

A comparison for values of the parameters that are of more interest for the present paper is given in table 2, where the most unstable eigenvalue and the axial wavenumber of the most unstable eigenvalue are reported for values of the parameters of experiments 6, 9 and 10 of CGH. In these experiments ζ, J^* and m are taken fixed to the values 1, 2102 and 0.0532 respectively, while a and Re_1 are varied. Our computations are compared with the data reported in PCJ, for which a similar numerical procedure was employed with a lower number of collocation points. The results in table 2 show that the agreement for both the maximum growth rate and the axial wavenumber of the maximum growth rate is generally quite good (all figures of our calculations are significant). However, there is a remarkable difference between our computation and the value reported by PCJ for the single case of the most unstable eigenvalue for the parameters of experiment 10. We carefully checked the convergence of our result, obtaining the same value with different numbers of collocation points and with the two different versions of our code. As a further

https://doi.org/10.1017/jfm.2014.155 Published online by Cambridge University Press

https://doi.org/10.1017/jfm.2014.155 Published online by Cambridge University Press

	N_1	N_2	c_1	c_2	c_3
Hu & Joseph (1989)	10	10	$0.38425 + 0.020753\mathrm{i}$	$0.66929 + 0.0041341\mathrm{i}$	$0.67251 + 0.0032652\mathrm{i}$
Hu & Joseph (1989)	15	15	$0.38451 + 0.020912\mathrm{i}$	$0.66932 + 0.0041366\mathrm{i}$	$0.67268 + 0.0032688\mathrm{i}$
Hu & Joseph (1989)	20	20	$0.38614 + 0.020874\mathrm{i}$	$0.66934 + 0.0041374\mathrm{i}$	$0.67274 + 0.0032702\mathrm{i}$
Present work	10	10	—	$0.66933 + 0.0041537\mathrm{i}$	$0.67274 + 0.0032806\mathrm{i}$
Present work	15	15	$0.38485 + 0.021479\mathrm{i}$	$0.66939 + 0.0041406\mathrm{i}$	$0.67285 + 0.0032735\mathrm{i}$
Present work	20	20	$0.38486 + 0.020963\mathrm{i}$	$0.66939 + 0.0041406\mathrm{i}$	$0.67285 + 0.0032735\mathrm{i}$
Present work	50	50	$0.38486 + 0.020973\mathrm{i}$	$0.66939 + 0.0041406\mathrm{i}$	$0.67285 + 0.0032735\mathrm{i}$
Present work	80	80	$0.38486 + 0.020973\mathrm{i}$	$0.66939 + 0.0041406\mathrm{i}$	$0.67285 + 0.0032735\mathrm{i}$

TABLE 1. Convergence history of the most unstable eigenvalue for the pseudospectral code employed in the present paper and comparison with the results presented in Hu & Joseph (1989). Details on the values of the parameters employed are given in the text.

	a	Re_1	k_{PCJ}	ω_{iMAX}^{PCJ}	k	ω_{iMAX}
CGH exp. 6	1.5	406.90	0.22	5.8597×10^{-3}	0.2266	5.9524×10^{-3}
CGH exp. 9	1.81	795.97	0.023	5.3989×10^{-4}	0.02468	5.3848×10^{-4}
CGH exp. 10	2.65	433.70	0.11	1.8272×10^{-2}	0.09575	9.7256×10^{-4}

TABLE 2. Comparison between the computations of Preziosi *et al.* (1989) and the pseudospectral code employed in the present paper. Here, ω_{iMAX}^{PCJ} and k_{PCJ} are the maximum growth rate and its associated wavenumber, respectively, reported by Preziosi *et al.* (1989), while ω_{iMAX} and k are calculated with our pseucospectral code.

check of our numerical result, we reproduced the data contained in table 2 of Hu & Joseph (1989), pertaining to the same set of experiments and reporting the values of various terms of the energy balance of the perturbed flow, calculated with a different numerical discretization. We were able to reproduce their results with reasonable accuracy (our computations of the energy terms are based on slightly different eigenfunction–eigenvalue couples, due to the different accuracy in the determination of the wavenumber of maximum growth rate), including the values for experiment 10 of CGH. Since the difference between the two computations in table 2 of the present paper relative to the maximum growth rate for the parameters of experiment 10 is of more than one order of magnitude, we suspect a misprint in the compilation of table 1 of PCJ.

3. Results

3.1. *Analysis of classical experiments*

The results presented in this section refer to the parameter values employed in experiments 6, 9 and 10 of CGH. The two fluids are assumed to have the same density and, in order to match the experimental conditions of CGH, the parameters J^* and m will be taken fixed to the values $J^* = 2102$ and $m = 0.0532$ respectively. Hence, the analysis has been made by varying a and the Reynolds number. For experiments 6, 9 and 10 the values of (a, Re_1) are (1.5, 406.9), (1.81, 795.97) and (2.65, 433.70) respectively.

For the parameters considered here the flow is asymptotically unstable only for axisymmetric modes, $n = 0$. In figure 2 the maximum growth rate for axisymmetric disturbances is reported as a function of the axial wavenumber k. It is clearly visible that the maximum growth rates, in particular for experiments 9 and 10, are very small in the dimensionless units employed here, $O(10^{-4})$, so these disturbances need a very long time to grow significantly.

The colour map in figure 3 reports the growth rate of the most unstable eigenvalue as a function of the axial wavenumber and the core Reynolds number for $a = 1.5$. The Reynolds number value of experiment 6 is highlighted with a horizontal line. The continuous black line corresponds to the marginal stability curve computed with our psuedospectral code. By comparing the present numerical results with the marginal curves reported by PCJ we note some discrepancies in the location of the marginal curve at high Reynolds numbers, although both calculations agree in determining the disturbance wavenumber that leads to the maximum growth rate. In order to investigate this discrepancy we recomputed the marginal curves by employing a lower number of collocation points, N, since the spectral code employed by PCJ is based on a three-equation formulation and uses $N \simeq 14$. The result of this low

https://doi.org/10.1017/jfm.2014.155 Published online by Cambridge University Press

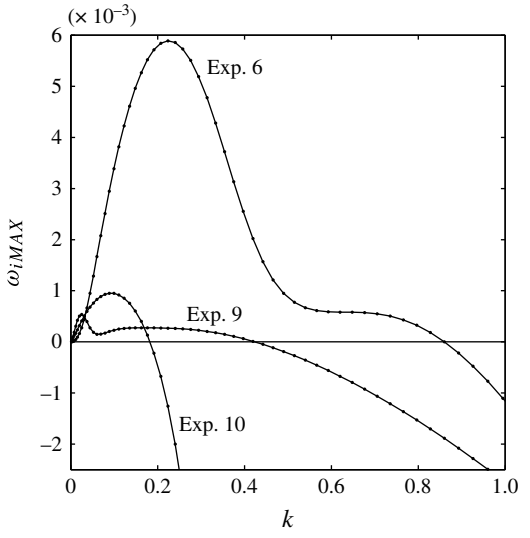


FIGURE 2. Maximum growth rate of the most unstable axisymmetric mode as a function of axial wavenumber k for experiments 6, 9 and 10 of Charles *et al.* (1961).

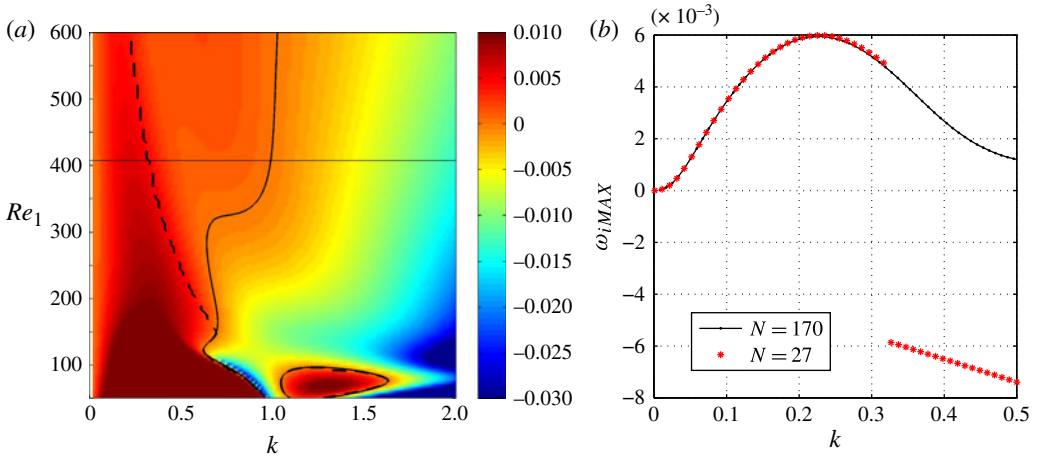


FIGURE 3. (*a*) Maximum growth rate of the most unstable axisymmetric disturbances as a function of the axial wavenumber k and Reynolds number of the core Re_1 for $a = 1.5$. The continuous black line corresponds to the marginal stability curve obtained using our pseudospectral code while the dashed line corresponds to the marginal stability curve obtained with a low-accuracy calculation. (*b*) Maximum growth rate curve as a function of the axial wavenumber k for experiment 6. In this figure the curve obtained using $N = 170$ collocation points is compared with the one obtained with $N = 27$ collocation points.

accuracy computation is the dashed black line in figure 3(*a*), which is qualitatively very similar to that displayed in figure 16 of PCJ (note that our scales are different and narrower than those employed in figure 16 of PCJ). In figure 3(*b*) a detail of the maximum growth rate as a function of the axial wavenumber is reported for the values of Re_1 relative to experiment 6. We note that the low number of collocation points dramatically deteriorates the accuracy of the calculations as k grows.

https://doi.org/10.1017/jfm.2014.155 Published online by Cambridge University Press

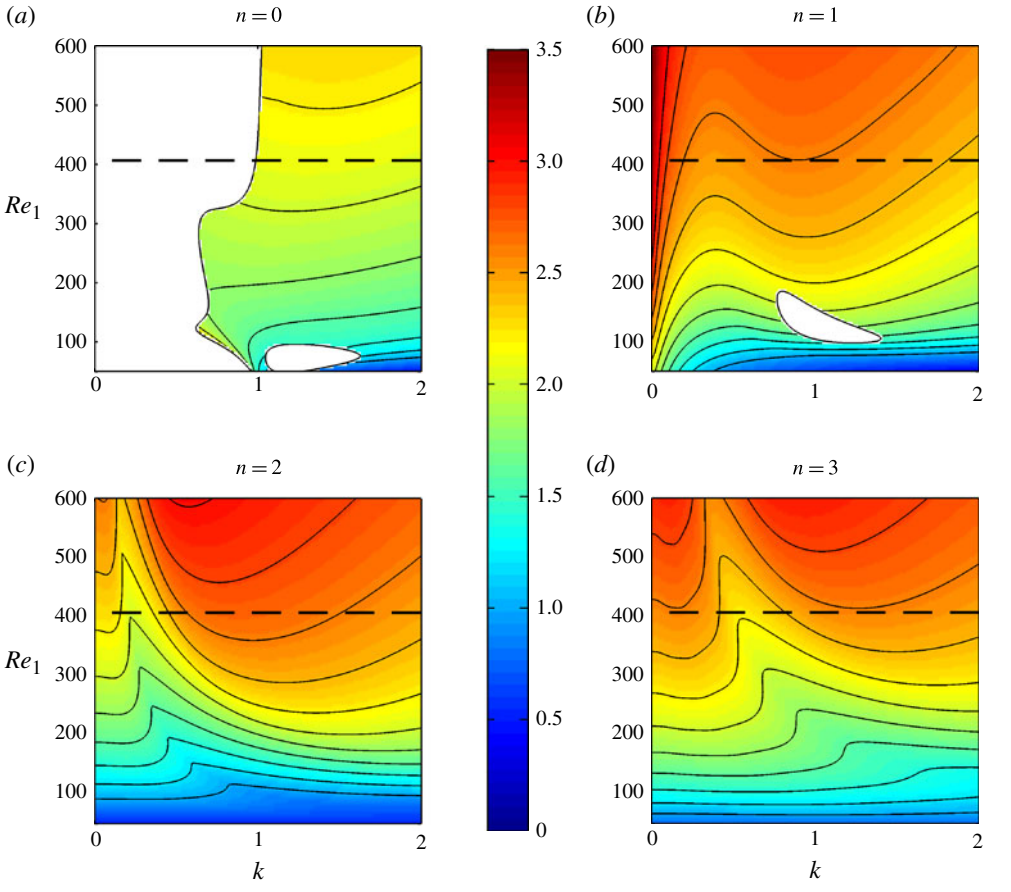


FIGURE 4. Logarithm to base 10 of the maximum non-modal amplification energy G_{MAX} as a function of the axial wavenumber k and the Reynolds number Re_1 for $a = 1.5$. The blank areas represent the region of modal instability.

The results of non-modal analysis for experiment 6 are reported in figures 4 and 5. The colour maps in figure 4 represent the logarithm to base 10 of the maximum value reached by the growth function, G_{MAX}, over different values of k and Re_1 and for the first four azimuthal wavenumbers. The blank portion of the figures relative to $n = 0$ and $n = 1$ represents the region of exponential instability, for which $G(t)$ is unbounded. In this and all the cases studied in this paper, long waves of non-axisymmetric disturbances are affected by significant transient amplifications, which increase with increasing Re_1. The maximum values of the transient growth at the experimental Reynolds number are reported in figure 5. This figure shows that in the experimental conditions the flow is affected by both (slow) exponential instability at $n = 0$ and $k < 1$ and significant transient growth at $n \neq 0$ and roughly the same values of k. The maximum transient growth is attained by the $n = 1$ mode in the limit of infinitely long waves, $k \to 0$.

The plot of G_{MAX} already illustrated does not give any information about the characteristic times of growth of the energy. In the presence of exponential instabilities, the physical relevance of such non-exponentially growing disturbances at different wavenumbers has to be carefully investigated. In order to balance

https://doi.org/10.1017/jfm.2014.155 Published online by Cambridge University Press

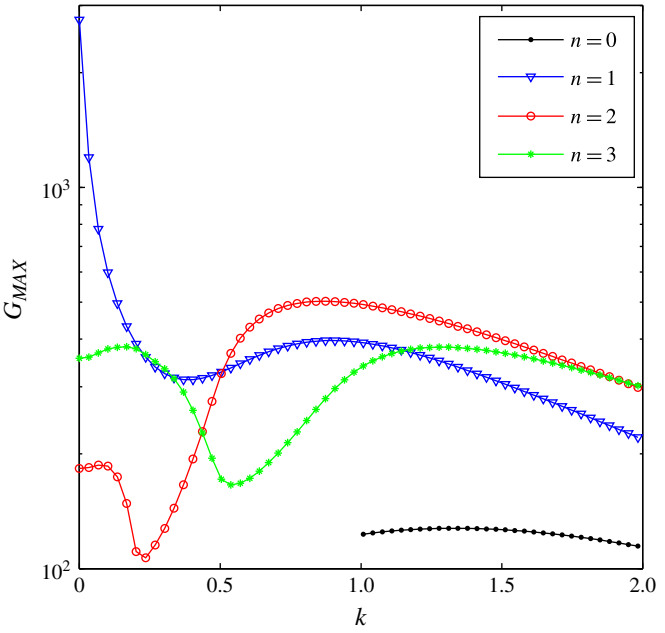


FIGURE 5. (Colour online) Maximum non-modal energy amplification G_{MAX} as a function of the axial wavenumber k for $Re_1 = 406.9$, $a = 1.15$ and for $n = 0, 1, 2, 3$.

the effects of non-normality and asymptotic instability, a comparison between the energy amplification curves of different disturbances is reported in figure 6(*a*). For each azimuthal wavenumber n, the growth function $G(t)$ is plotted for an axial wavenumber k that is chosen as the most unstable one for $n = 0$ or as the one for which disturbances attain the maximum value of G_{MAX} among all wavenumbers at the same n for $n > 0$. Figure 6(*a*) shows that the fastest exponentially unstable disturbance at $n = 0$ actually grows very slowly in time, as compared with spiral disturbances which reach high levels of energy (roughly one order of magnitude higher) at intermediate times. Figures 6(*b*) and 6(*c*) report the analogous comparison for the parameter values relative to experiments 9 and 10 respectively. These plots not only confirm the picture reported in figure 6(*a*), but actually further evidence from a quantitative viewpoint the relevance of transient growth of non-axisymmetric disturbances at intermediate times. For both cases the energy levels attained by spiral disturbances are two orders of magnitude greater than those attained by axisymmetric disturbances for several decades of non-dimensional time units. For experiment 6 the growth of the planar disturbance $n = 1$, $k = 0$ is crossed by the exponential growth of the most unstable mode at the non-dimensional time $t \simeq 413$. The analogous values for experiments 9 and 10 are $t \simeq 6810$ and $t \simeq 4035$ respectively.

Two more considerations can be made about the plots in figure 6. The first is that non-normality of the governing operator affects not only the stable spiral disturbances, as is expected, but also the axisymmetric unstable ones. The evolution of an exponentially unstable disturbance should, in fact, be linear in the logarithmic scales of figure 6, while in the plots this linear evolution establishes only asymptotically after an initial transient modulation. The influence of non-normality on these unstable disturbances is, however, very weak, as is usual for axisymmetric disturbances of other canonical flows (e.g. HP flow). The second consideration is that the comparison

https://doi.org/10.1017/jfm.2014.155 Published online by Cambridge University Press

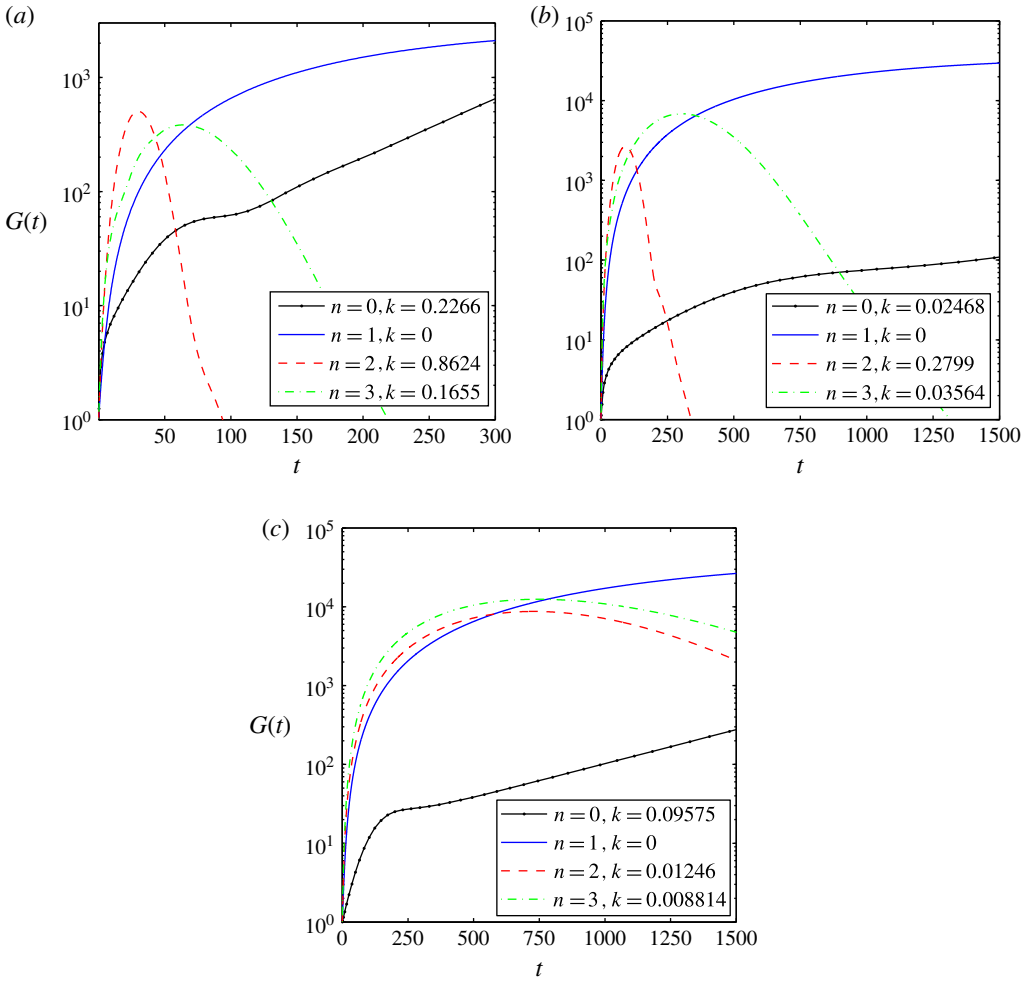


FIGURE 6. (Colour online) The transient growth function of the most unstable mode for $n = 0$ and for the axial wavenumber that reaches the highest value of G_{MAX} for $n > 0$. (*a*) Parameters from experiment 6 ($Re_1 = 406.9$, $a = 1.5$), (*b*) experiment 9 ($Re_1 = 795.97$, $a = 1.81$), (*c*) experiment 10 ($Re_1 = 433.7$, $a = 2.65$).

between the growth functions of different spiral disturbances shows that the relevance of non-axisymmetric modes is governed not only by the maximum value reached by $G(t)$ but also by the characteristic times of growth. Figure 6, for example, shows that although the maximum transient growth is obtained by the $n = 1$, $k = 0$ spiral disturbance, this maximum is reached after a very long time which is of the order of the crossing time with the growth function of the unstable disturbance. There is a large interval of intermediate times in which other spiral disturbances reach comparable high values of energy and are hence of the same importance from the point of view of energy amplification.

In order to give an overall picture of the relevance of these spiral disturbances as compared with the axisymmetric unstable ones, in figure 7 the colour map of the logarithm to base 10 of the energy amplification G as a function of the non-dimensional time t is reported for a range of axial wavenumbers k at different

https://doi.org/10.1017/jfm.2014.155 Published online by Cambridge University Press

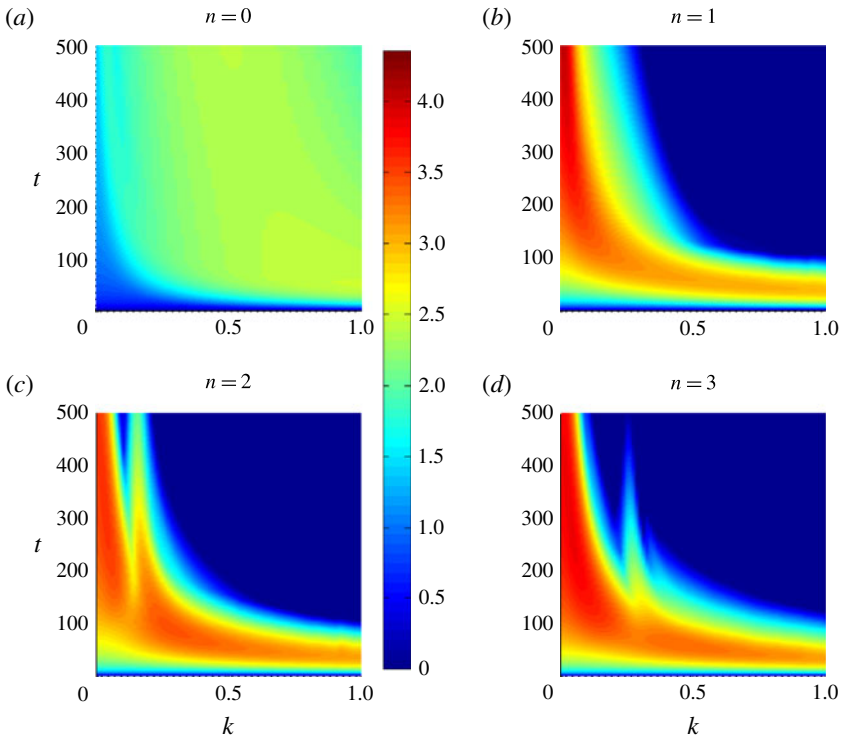


FIGURE 7. Logarithm to base 10 of the energy amplification G as a function of the non-dimensional time t and the axial wavenumber k at $Re_1 = 795.97$ and $a = 1.81$ (experiment 9).

azimuthal wavenumbers n. The values of the parameters Re_1 and a are relative to experiment 9 of CGH. The figure shows that there is a band of axial wavenumbers, mainly pertinent to long waves, that is strongly affected by non-normality at all the spiral disturbances we investigated and for which the levels of energy amplification are comparable. One can also observe that in some situations there are two lobes in the maps, indicating two families of modes at different ranges of k growing at different rates. This occurrence can be inferred also by the plots of G_{MAX} of figure 5 relative to the parameters of experiment 6.

As illustrated by the formula (2.7), the disturbance energy is composed of three terms: the kinetic energy, E_K, of the core, the kinetic energy of the annulus and an energy term associated with surface tension, E_T. In fact, this last term gives information on the evolution of the surface area with respect to the cylinder with mean radius of the perturbed core. In figure 8 these three components are separately reported for the time evolution of the initial condition constituted by the optimal perturbation relative to $k = 0.8624$ and $n = 2$ for experiment 6. The gain function of the disturbances relative to these parameters is given by the dashed curve in figure 6(*a*). Figure 8 shows that all the energy amplification is clearly related to the annular phase, while the term associated with surface tension is negligible. This situation is typical for all the transiently growing spiral disturbances we illustrated. More comments on the energy budget for CAF are given in § 3.3.

This conclusion can be obtained from a different perspective by inspecting another classical tool of non-modal analysis which is the ϵ-pseudospectrum (Trefethen &

https://doi.org/10.1017/jfm.2014.155 Published online by Cambridge University Press

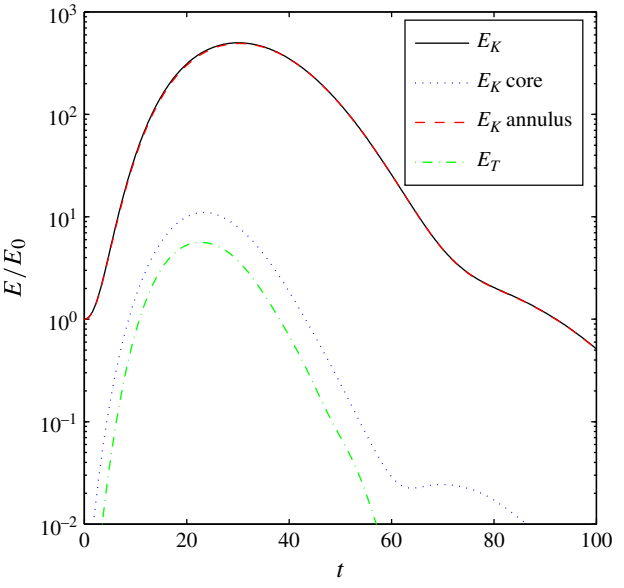


FIGURE 8. The kinetic and surface energy components of the optimal perturbation for the disturbance with $n = 2$ and $k = 0.8624$ for the parameters of experiment 6.

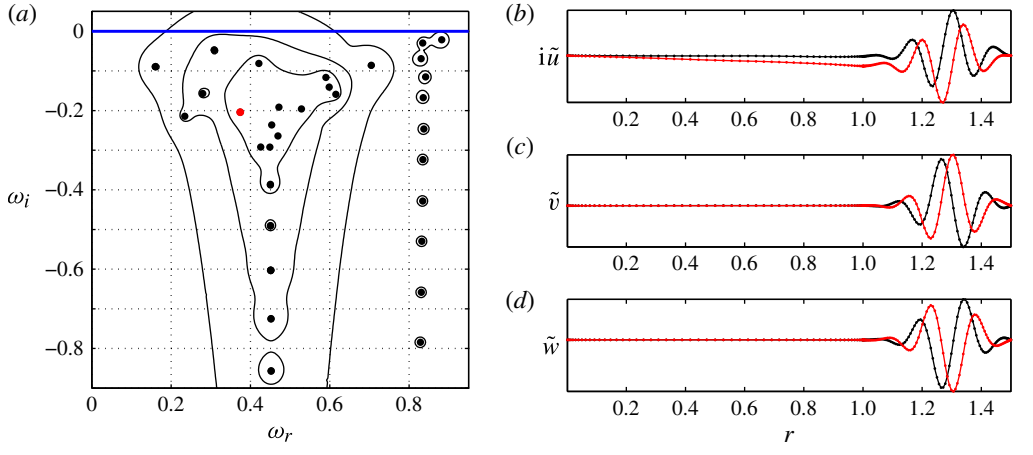


FIGURE 9. (*a*) Boundaries of the ϵ-pseudospectrum of the linearized operator for $Re_1 = 406.9$, $k = 0.8624$ and $n = 2$. From the outside to the inside, the curves correspond to $\epsilon = 10^{-2}$, 10^{-3}, 10^{-4}. (*b*) From top to bottom, the real (black lines) and the imaginary (red lines) parts of the eigenfunctions of the three velocity components, $\mathrm{i}\tilde{u}$, $\tilde{v}$, $\tilde{w}$, relative to the eigenvalue marked in red in (*a*).

Embree 2005). In figure 9(*a*), the spectrum and the ϵ-pseudospectrum of the linearized governing operator are reported for the same parameters as the red curve in figure 6(*a*). The spectrum is constituted of two branches, both containing only stable eigenvalues. The left part, which has the classical three-branch structure of both HP flow and the Orr–Sommerfeld operator, is the one that is strongly affected by non-normality.

https://doi.org/10.1017/jfm.2014.155 Published online by Cambridge University Press

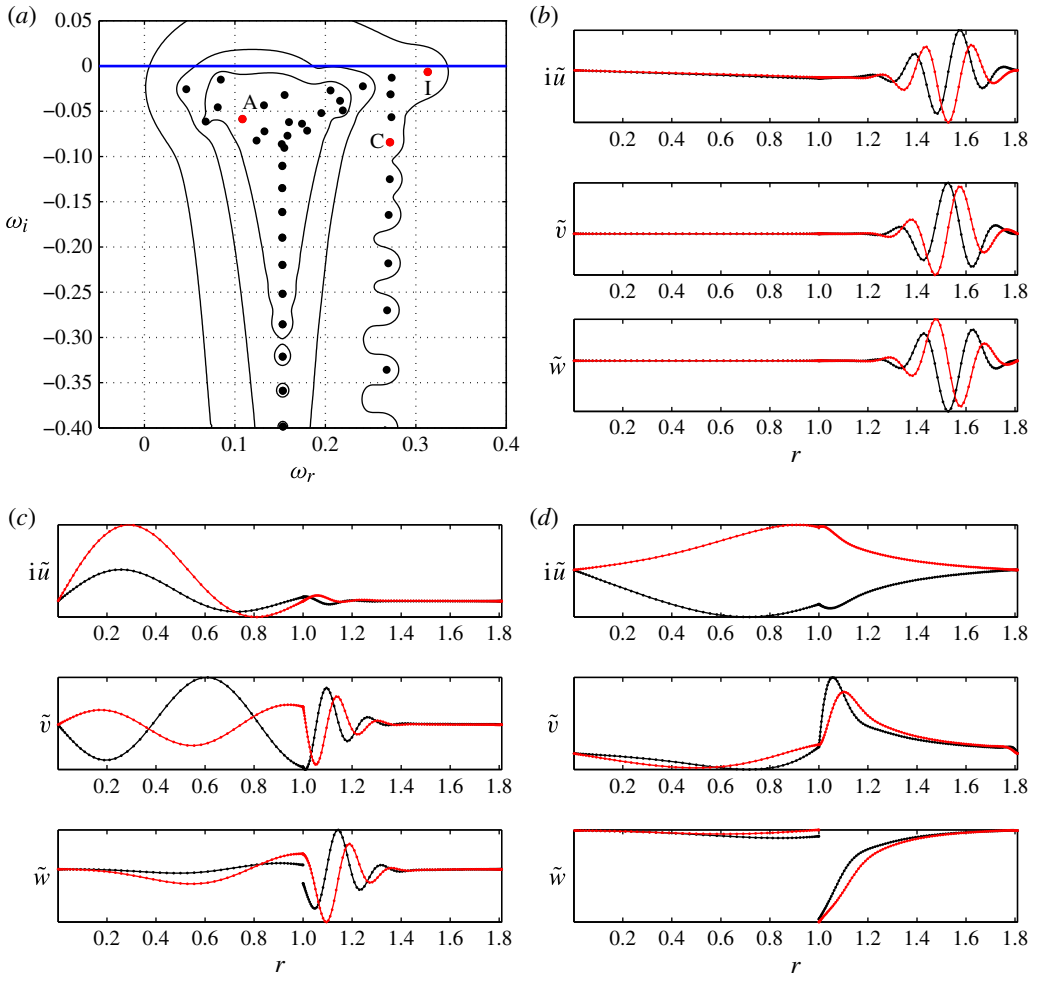


FIGURE 10. (*a*) Boundaries of the ϵ-pseudospectrum of the linearized operator for $Re_1 = 795.97$, $k = 0.27987$ and $n = 2$. From the outside to the inside, the curves correspond to $\epsilon = 10^{-2}$, 10^{-3}, 10^{-4}. (*b*) Real (black lines) and imaginary (red lines) parts of the eigenfunctions of the three velocity components, $\mathrm{i}\tilde{u}$, $\tilde{v}$, $\tilde{w}$, relative to the eigenvalue labelled A, annular mode. (*c*) Real (black lines) and imaginary (red lines) parts of the eigenfunctions relative to the eigenvalue labelled C, core mode. (*d*) Real (black lines) and imaginary (red lines) parts of the eigenfunctions relative to the eigenvalue labelled I, interfacial mode.

In figure 9(*b*) the components of velocity eigenfunctions pertinent to one of the eigenvalues of this branch (marked as a red dot in figure 9*a*) are reported. The shape of these eigenfunctions shows that much of the structure is contained in the annular region, $r > 1$. From this we deduce that the left branch of the spectrum, with which non-orthogonal eigenmodes are associated, is relative to the annular less viscous phase. A more complete picture of the classification of the various parts of the spectrum is given in figure 10, relative to the azimuthal wavenumber $n = 2$ and the axial wavenumber attaining the maximum value of G for the parameters of

https://doi.org/10.1017/jfm.2014.155 Published online by Cambridge University Press

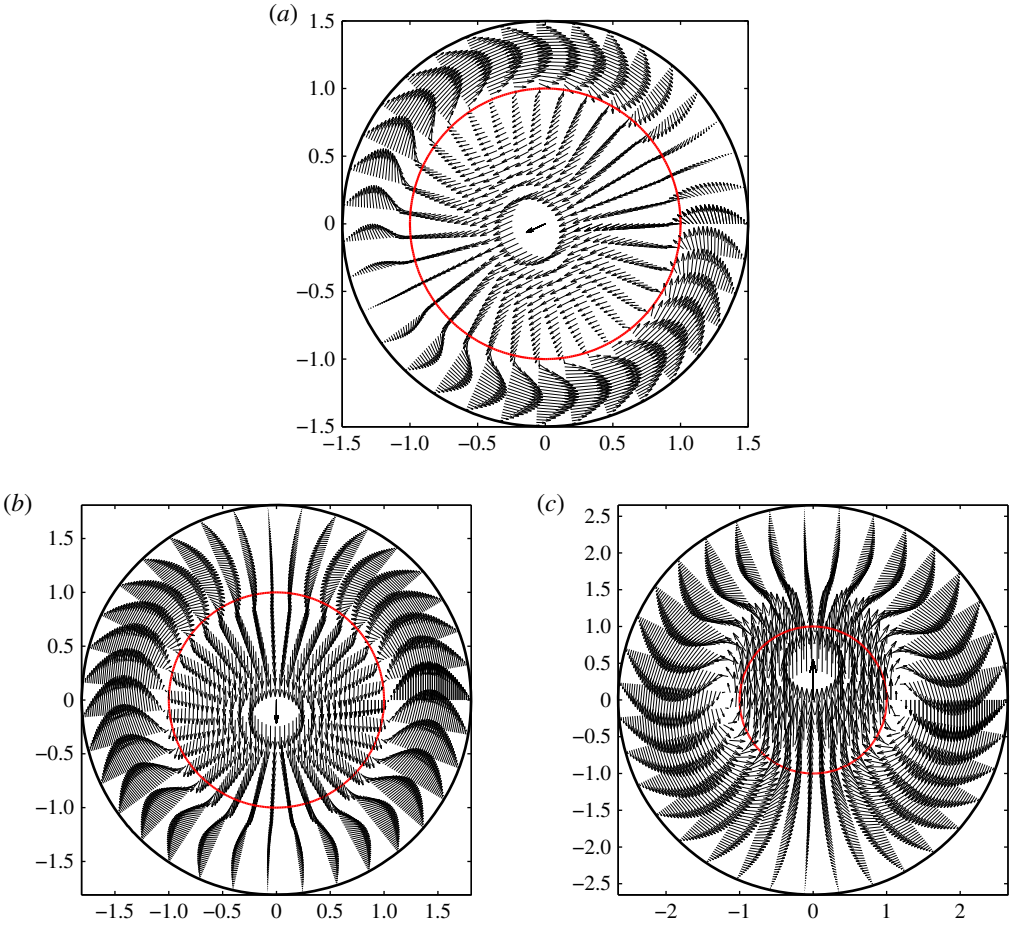


FIGURE 11. (Colour online) Optimal perturbations for $n = 1$ and $k = 0$ for the three experimental conditions considered: (*a*) experiment 6, (*b*) experiment 9, (*c*) experiment 10.

experiment 9. In this plot three families of eigenvalues are identified, labelled A, annular mode, C, core mode, and I, interfacial mode.

In figure 11 the optimal perturbations for the disturbances relative to $n = 1$ and $k = 0$ are reported for the three experiments considered in this section. Again, one can observe that such optimal perturbations have their maximum intensity in the annular region and, as the area of this region increases, they tend to the classical structure documented for the HP flow, constituted of a pair of counter-rotating vortices.

As a final comment, one can observe that the conditions of the experiments of CGH are quite far from the real conditions of interest in applications, where the viscosity ratios are usually much lower than those considered by CGH (also by more than one order of magnitude) and where the Reynolds number can be significantly higher. In such a situation it seems natural to investigate the scaling of the maximum value attained by the growth function G as m and Re_1 increase. This has been carried out for the case of an $n = 1$, $k = 0$ disturbance for a CAF with $a = 1.81$ and the radius ratio of experiment 9, and by varying both the viscosity ratio m and the core Reynolds

https://doi.org/10.1017/jfm.2014.155 Published online by Cambridge University Press

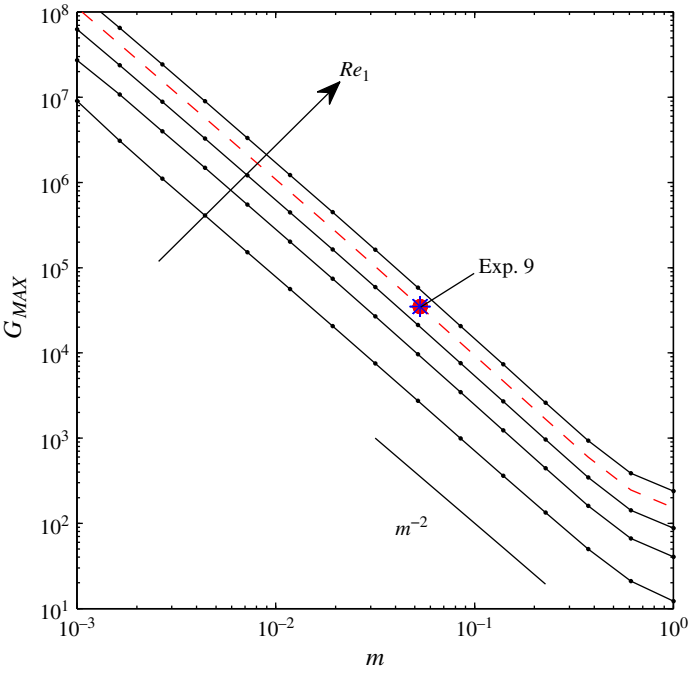


FIGURE 12. (Colour online) Values of G_{MAX} for the $n=1$, $k=0$ perturbation as a function of the viscosity ratio m and for values of Re_1 of 200, 400, 600, 795.97 and 1000. The radius ratio is $a=1.81$. The dashed curve corresponds to $Re_1=795.97$.

number Re_1. The results are reported in figure 12, where the experimental conditions of experiment 9 (i.e. $Re_1 = 795.97$ and $m = 0.0532$) are highlighted with a starred dot. The figure shows that the maximum value of G strongly increases with m and Re_1, thus leading to the conclusion that for values of the parameters of interest for real applications the mechanism of non-modal energy growth discussed up to now is enhanced and its relevance should be much more pronounced. The plot also shows that the maximum value of G displays a scaling law with m that is remarkably consistent with a power law with exponent -2. Note that for a fixed value of the core Reynolds number, a scaling law with m corresponds to a scaling law with the inverse of the annular Reynolds number Re_2, since for an equal density CAF the relation $Re_1/Re_2 = m$ holds. Hence, the scaling law m^{-2} can be interpreted as a scaling of G_{MAX} with Re_2^2. Similar behaviour has been detected for single-fluid canonical flows (e.g. Schmid & Henningson 1994).

3.2. *Comparison with more recent experiments*

The analysis performed in the previous section pertains to classical experiments for which a large number of theoretical and numerical results are present in the literature. In this section, the relevance of the presented investigation is strengthened by considering more recent experiments, for which the occurrence of both dispersed and stable flows in a CAF configuration is documented. The comparison of the results of our modal and non-modal analysis with the global characteristics of the flows in the different regimes is intended to give support to the conclusions of the

https://doi.org/10.1017/jfm.2014.155 Published online by Cambridge University Press

previous section and to furnish new insights into the physical mechanisms underlying the phenomenology.

The literature on experimental studies of CAF configurations in horizontal pipes is quite extensive. For most of these studies, however, a detailed comparison with theoretical results of PCAF is quite difficult, if not impossible. In many cases the experiments were carried out by considering phases having a significant density difference. This led to asymmetries in the flow, with the heavier fluid tending to arrange itself near the bottom of the pipe, and thus preventing the formation of an annular flow. Moreover, most of these studies were focused on the determination of flow pattern maps, with insufficient observation and description of the transition process towards stratified, annular or dispersed flow configurations.

Among the few studies in which these issues are less critical, we considered for our analysis the experimental study by Sotgia, Tartarini & Stalio (2008). The experiments described in that paper were conducted on the horizontal pipe flow of a mixture of mineral oil and tap water with the density ratio ζ kept fixed to a value of ~ 1.11, leading to mild asymmetry in the flow. The viscosity ratio m had a value of $\sim 1.11 \times 10^{-3}$, which is of more interest for applications. Moreover, a set of quite clear pictures of the flow patterns, obtained by illuminating the transparent pipes carrying the flow with high intensity light sources, was reported.

The case analysed here is the experimental campaign conducted with a 26 mm Plexigas pipe in which the flow pattern evolves from dispersed to corrugated annular configuration when the oil's superficial velocity J_o is kept constant at the value 0.88 m s^{-1} and the water's superficial velocity J_w is varied between the values 2.51 and 0.05 m s^{-1}. This series of experiments, which is illustrated in figure 6 of Sotgia *et al.* (2008), has been chosen because, for the values of the oil flow rate considered, the asymmetries in the flow are less pronounced and a stratified flow configuration never appears. We also investigated other experiments documented in the paper, obtaining qualitatively similar results.

Figures 6(a) and 6(c) of Sotgia *et al.* (2008) report two different flow patterns, obtained by reducing J_w from the value 2.51 to 0.36 m s^{-1}. The first figure, relative to the case $J_w = 2.51$ m s^{-1}, displays a dispersed flow pattern in which the oil core is in the form of drops dispersed in the continuous water phase. The non-dimensional parameters characterizing this flow regime are $a = 2.59$, $Re_1 = 28.659$ and $J^* = 0.2737$, corresponding to a surface tension coefficient measured as $T = 0.02$ N m^{-1}. Equations (13.1)–(13.2) reported by PCJ have been used to convert the data given by Sotgia *et al.* (2008) into the parameters used in our analysis. The second figure, relative to the case $J_w = 0.36$ m s^{-1}, displays an annular flow pattern with a wavy or corrugated interface of separation between the two phases. The non-dimensional parameters are now $a = 1.35$, $Re_1 = 14.935$ and $J^* = 0.2737$. The wavy pattern on the interface can be seen to have a wavelength (measured as the distance between two successive wave crests) which is roughly of the same order of the pipe radius, hence corresponding to a non-dimensional wavenumber $k \simeq 2\pi/a \simeq 4.8$.

In order to investigate these different flow patterns, we computed the maximum growth rates for the two cases as functions of the non-dimensional axial wavenumber k and for the first four azimuthal wavenumbers n. Figures 13(a) and 13(b) show that in both cases the flow is affected by modal instability at all the azimuthal wavenumbers considered, except for the $n = 3$ disturbance relative to the dispersed case. The instabilities peak at k between 2.13 and 2.52 for the dispersed case and between 4.05 and 4.78 for the wavy case. This last result can be considered to be in line with the experimental findings, since the wavenumber of the most

https://doi.org/10.1017/jfm.2014.155 Published online by Cambridge University Press

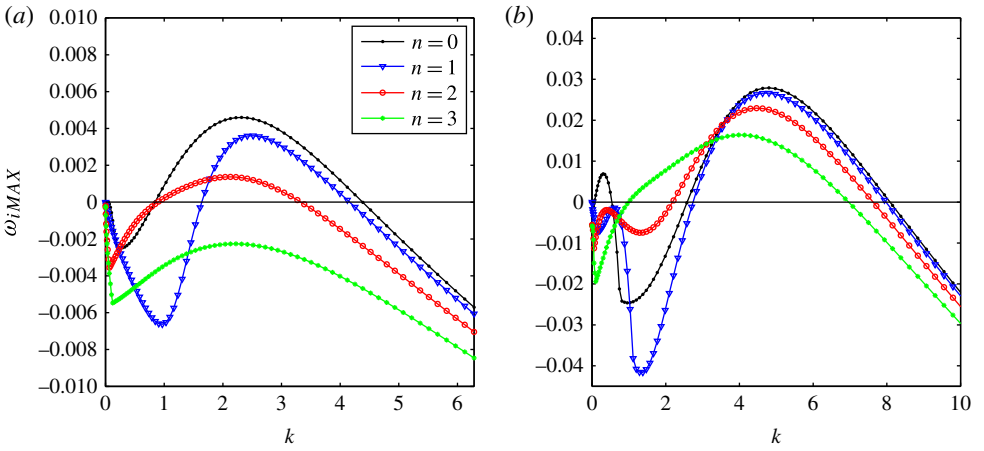


FIGURE 13. (Colour online) Growth rates as functions of k and for the first four azimuthal wavenumbers for the cases of (*a*) the dispersed flow pattern presented in figure 6(*a*) of Sotgia *et al.* (2008) and (*b*) the wavy annular flow pattern presented in figure 6(*c*) of Sotgia *et al.* (2008). The exact values of the non-dimensional parameters are given in the text.

unstable mode agrees reasonably with the empirically estimated wavenumber of the corrugation of the interface. In making this comparison we implicitly assume that the exponential growth of interface disturbances undergoes a saturation, due to nonlinear effects, once the wave amplitude becomes finite. In these cases the linearly unstable flow typically reduces to a stable configuration characterized by finite amplitude corrugations (Papageorgiou, Maldarelli & Rumschitzki 1990; Miesen *et al.* 1992). The dispersed configuration is not completely explained by this analysis, since the presence of weaker unstable modes (one order of magnitude smaller) with the same characteristics would suggest a similar corrugated final configuration also for the parameters of the case presented in figure 6(*a*) of Sotgia *et al.* (2008).

Non-modal analysis gives some indications on the possible reasons for this weakness of modal theory, since the computation of maximum transient growth shows the presence of strong algebraic amplifications of the energy of spiral disturbances with vanishing axial wavenumbers. In figure 14 the transient growth of the disturbance corresponding to the most unstable wavenumber is compared with the growth function of the $n = 1$, $k = 0$ disturbance (which is stable with vanishing growth rate). The figure shows that the two cases (dispersed and wavy annular) are characterized by a different balance between algebraic and exponential growth functions. In the first case analysed in figure 14(*a*) (for the dispersed configuration) the growth function of the stable disturbance reaches values much higher than those of the exponentially unstable disturbance (up to two orders of magnitude) for a significant time interval. On the other hand, figure 14(*b*) (for the corrugated configuration) shows a situation in which the energy of the stable spiral disturbance has much lower values and is quickly overcome by the exponentially divergent disturbance. Note that a different time interval is employed for the two plots. At $t = 500$ the curve for the spiral disturbance in figure 14(*b*) has almost reached its maximum value, which is around 4.5×10^3, while at $t = 1500$ the spiral disturbance of figure 14(*a*) is still growing toward its maximum and overtakes the value 10^5 at around $t = 2000$. An estimate of the

https://doi.org/10.1017/jfm.2014.155 Published online by Cambridge University Press

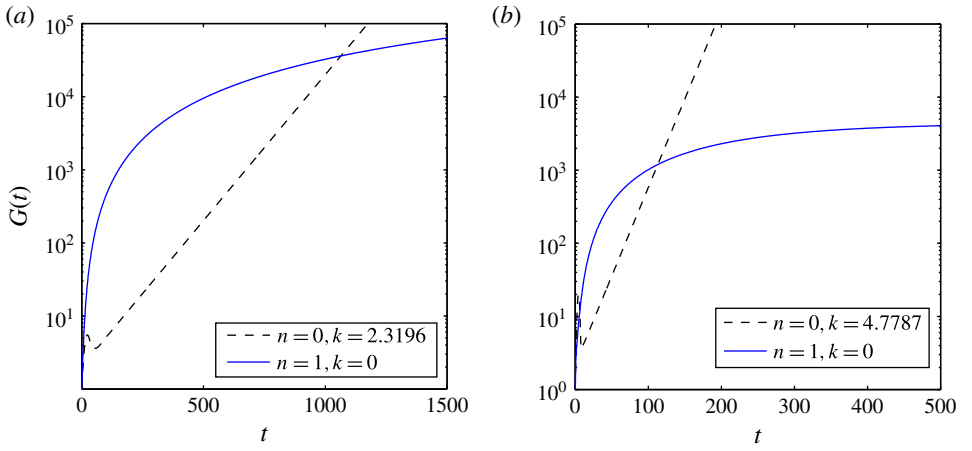


FIGURE 14. (Colour online) Transient growth functions of the most unstable mode for $n=0$ and of the disturbance that reaches the highest value of G_{MAX} for $n=1$: (*a*) $a=2.59$, $Re_1=28.659$ and $J^*=0.2737$; (*b*) $a=1.35$, $Re_1=14.935$ and $J^*=0.2737$.

non-dimensional time scales relevant for the problem can be obtained by comparing the reference time employed in the non-dimensionalization and the characteristic times of the experiment. For the case of the dispersed configuration, the centreline velocity and the core radius assume the values $W_0 = 5.901$ m s^{-1} and $R_1 = 5 \times 10^{-3}$ m; hence, the reference time for this case is of the order of one millisecond. From the experimental details reported in Sotgia *et al.* (2008) we learn that the photographic visualization of the flow is obtained at a distance of 8 m from the inlet and hence the experimental time scale is of the order of seconds. This clarifies that the emphasis on non-dimensional time scales of the order of thousands is not misplaced.

3.3. *Energy budget*

In order to gain more insight into the origin of the documented strong amplification of energy in stable disturbances, in this section we derive the equation for the energy evolution in time for CAF. The Reynolds–Orr equation, conveniently modified to account for the boundary and interface conditions, has been used. By multiplying the linearized momentum equations written for the generic Fourier mode by the complex conjugates of $\hat{u}$, $\hat{v}$, $\hat{w}$, and by subsequently integrating over r in the core and annular regions, one obtains

$$\begin{aligned}
&\frac{1}{2}\,\partial_t \sum_{l=1}^{2} \int_{\Omega_l} (|\hat{u}|^2 + |\hat{v}|^2 + |\hat{w}|^2) r \,\mathrm{d}r + \frac{1}{2}\frac{J}{Re_1^2}(n^2+k^2)\,\partial_t|\hat{\delta}|^2 - \frac{1}{2}\frac{J}{Re_1^2}\,\partial_t|\hat{\delta}|^2 \\
&\quad = -\mathrm{Re}\left\{ \mathrm{i} \sum_{l=1}^{2} \int_{\Omega_l} \overline{W}'(\hat{u}\,\hat{w}_*) r \,\mathrm{d}r \right\} + \left\langle \frac{1}{Re}\left(\hat{u}_*\partial_r(r\hat{u}) - 2\hat{u}_*\partial_r\hat{u} + \hat{v}_*\partial_r(r\hat{v}) + \hat{w}_*\partial_r\hat{w} \right) \right\rangle \\
&\qquad - \sum_{l=1}^{2} \int_{\Omega_l} \frac{1}{Re_l} \left\{ \frac{1}{r^2}|\partial_r(r\hat{u})|^2 + \frac{1}{r^2}|\partial_r(r\hat{v})|^2 + |\partial_r\hat{w}|^2 + \left(\frac{n^2}{r^2}+k^2\right) \right. \\
&\qquad \left. \times (|\hat{u}|^2 + |\hat{v}|^2 + |\hat{w}|^2) + \frac{4n}{r^2}\mathrm{Re}\{\hat{v}\hat{u}_*\} r \,\mathrm{d}r \right\} - \frac{1}{Re_1}(|\hat{u}(0)|^2 + |\hat{v}(0)|^2),
\end{aligned} \tag{3.1}$$

https://doi.org/10.1017/jfm.2014.155 Published online by Cambridge University Press

where interface and boundary conditions have been used in order to eliminate the pressure from the equation. Here, $\Omega_1 = [0, 1]$, $\Omega_2 = [1, a]$, an asterisk denotes complex conjugation and $\langle\cdot\rangle$ is the jump operator across the interface, i.e. $\langle f\rangle = f_1 - f_2$.

Equation (3.1) gives a relation for the evolution of the system energy in time. By adopting the notation of Hu & Joseph (1989), the following production and dissipation terms can be identified:

$$E_K = \frac{1}{2}\sum_{l=1}^{2}\int_{\Omega_l}(|\hat{u}|^2 + |\hat{v}|^2 + |\hat{w}|^2) r\,\mathrm{d}r, \tag{3.2}$$

$$E_T = \frac{1}{2}\frac{J}{Re_1^2}(n^2 + k^2)\,|\hat{\delta}|^2, \tag{3.3}$$

$$E_r = \frac{1}{2}\frac{J}{Re_1^2}\,|\hat{\delta}|^2, \tag{3.4}$$

$$I = \mathrm{Re}\left\{\mathrm{i}\sum_{l=1}^{2}\int_{\Omega_l}\overline{W}'(\hat{u}\,\hat{w}_*) r\,\mathrm{d}r\right\}, \tag{3.5}$$

$$B = \left\langle\frac{1}{Re}\left(\hat{u}_*\partial_r(r\hat{u}) - 2\hat{u}_*\partial_r\hat{u} + \hat{v}_*\partial_r(r\hat{v}) + \hat{w}_*\partial_r\hat{w}\right)\right\rangle, \tag{3.6}$$

$$D = -\sum_{l=1}^{2}\int_{\Omega_l}\frac{1}{Re_l}\left\{\frac{1}{r^2}|\partial_r(r\hat{u})|^2 + \frac{1}{r^2}|\partial_r(r\hat{v})|^2 + |\partial_r(\hat{w})|^2 + \left(\frac{n^2}{r^2} + k^2\right)\right.$$
$$\left.\times\,(|\hat{u}|^2 + |\hat{v}|^2 + |\hat{w}|^2) + \frac{4n}{r^2}\mathrm{Re}\{\hat{v}\hat{u}_*\} r\,\mathrm{d}r\right\} + \frac{1}{Re_1}(|\hat{u}(0)|^2 + |\hat{v}(0)|^2). \tag{3.7}$$

The left-hand side of (3.1) is the time variation of the total energy of the system, composed of the kinetic energy E_K and the potential energy associated with the surface tension. This last term is composed of the positive quantity E_T, already defined in § 2.1, and the term E_r, which is proportional to the reduction of the mean radius of the perturbed configuration with respect to the unperturbed cylindrical surface. The difference between these quantities is the increment in surface energy due to an interface perturbation. For long-wave axisymmetric disturbances this difference is negative and there is the potential for a capillary instability. Here, I is the rate at which the Reynolds stress transfers energy between the base flow and the perturbed flow. This term can either stabilize or destabilize, depending on the details of the problem. Here, D represents the viscous dissipation of the perturbed flow; it is always negative and hence opposes instability. These two last mechanisms are present also in one-fluid flows. Here, B represents the rate at which energy is supplied at the interface due to the work of the tangential stress. Since this term finds its origin in the jump of viscosity, and consequently of the base flow slopes at the interface, Hu & Joseph (1989) called it 'interfacial friction'. In conclusion, the possible sources of kinetic energy for the perturbations are the base flow through the term I and the interfacial friction mechanism through the term B. A capillary instability can arise only for axisymmetric disturbances having $k < 1$. In such cases a reduction of the total area of the interface can feed instability if the released energy is not completely dissipated or exchanged with the base flow. In what follows, the time evolutions of the various terms of the energy budget are presented with reference to some of the experiments documented by CGH and by Sotgia *et al.* (2008).

https://doi.org/10.1017/jfm.2014.155 Published online by Cambridge University Press

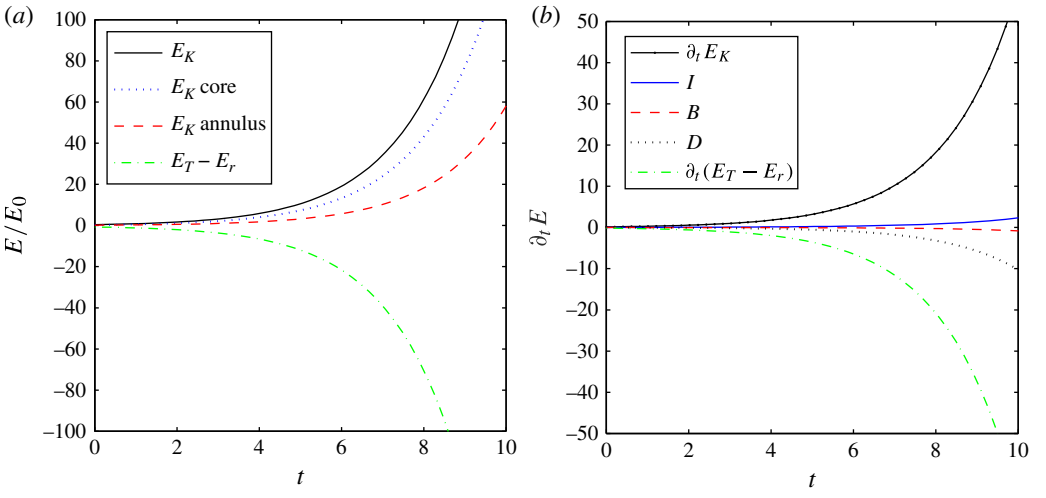


FIGURE 15. (Colour online) Time evolution of the components of the energy budget for the optimal perturbation at $n = 0$, $k = 0.6694$ relative to the parameters of experiment 4 of CGH: (*a*) kinetic and potential energy components; (*b*) rate of energy components.

As a starting point, let us consider a case in which classical eigenvalue analysis is successful in predicting the characteristics of the final stage of the instability. For the parameters of experiment 4 of CGH ($m = 0.0532$, $a = 2.24$, $\zeta = 1$, $Re_1 = 26.98$, $J^* = 2102$) the modal analysis performed by PCJ led to a good agreement with experimental results. The flow is unstable at long waves for axisymmetric disturbances and the instability has the characteristics of a capillary instability modified by shear. In figure 15 the various components of the energy budget are presented for the parameters of experiment 4. These curves have been calculated by evolving the linearized system of equations in time, starting from an initial condition chosen as the optimal perturbation for the most unstable axisymmetric disturbance, characterized in our case by the axial wavenumber $k = 0.6694$. Since the disturbance is unstable (and hence the growth function is unbounded), the optimal pertubation is calculated here as the initial perturbation gaining the maximum possible energy amplification at a long time, which in this case has been taken as $t = 20$. We verified that the details of the curves are not much influenced by the particular value assumed for the optimization time.

Figure 15(*a*) displays the evolution of the total kinetic energy, together with its core and annular components. The term $E_T - E_r$ is the surface energy. Note that, with the notation employed, negative values of $E_T - E_r$ imply instability. The figure shows a classical example of capillary instability, in which the energy released by the surface is converted to kinetic energy of the perturbation, which grows in both the core and annular phases, with a predominance in the core phase. The effects of viscosity and shear can be visualized by considering the time evolution of the various components of the rate of change of energy present in the energy budget.

Figure 15(*b*) shows that the influence of the dissipation term D and of the Reynolds stress and interfacial terms (I and B respectively) is quite modest. Dissipation adsorbes energy, mitigating the growth rate of the instability. The Reynolds stress term is destabilizing, while the interfacial friction has a weak stabilizing effect. In fact, the most important information stemming from these plots is that non-normality

https://doi.org/10.1017/jfm.2014.155 Published online by Cambridge University Press

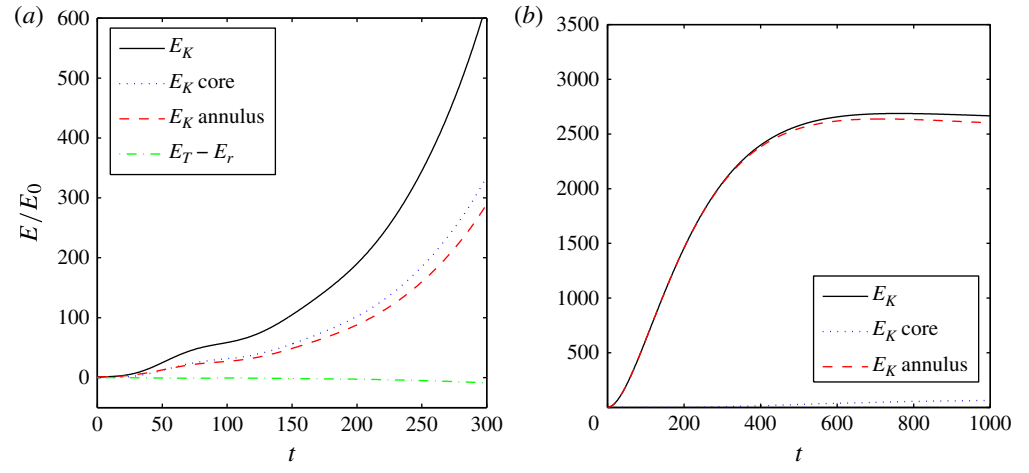


FIGURE 16. (Colour online) Time evolution of kinetic and potential energy components for optimal perturbations relative to the parameters of experiment 6 of CGH: (*a*) $n = 0$ and $k = 0.2266$; (*b*) $n = 1$ and $k = 0$.

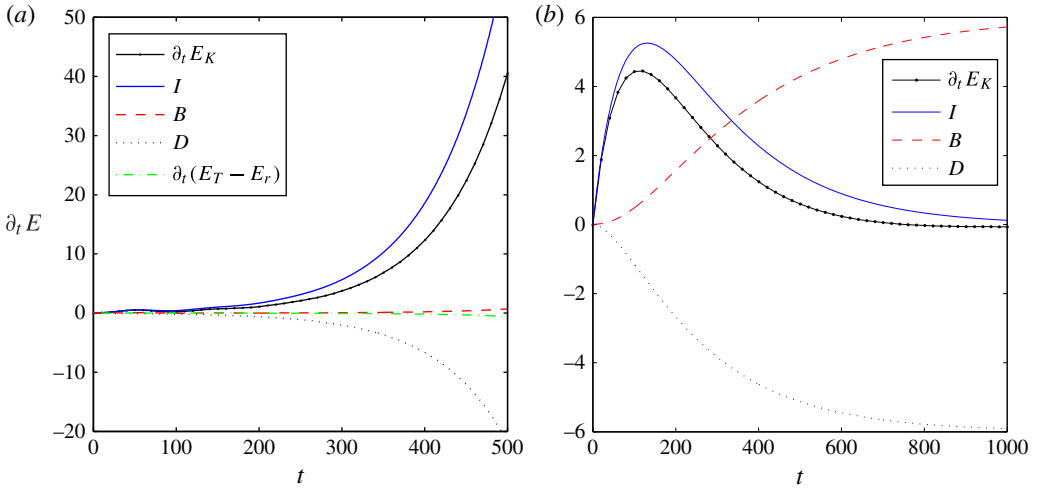


FIGURE 17. (Colour online) Evolution of the energy production and dissipation terms of the Reynolds–Orr equation for optimal perturbations relative to the parameters of experiment 6 of CGH: (*a*) $n = 0$ and $k = 0.2266$; (*b*) $n = 1$ and $k = 0$.

has a negligible effect on the instability. All the curves depicted in figure 15 are exponentials (they would appear as straight lines in a log plot) and transient effects are practically absent. In this respect, these results do not add any information to the analysis presented by Hu & Joseph (1989), in which the growth rates of the various terms have been computed within the frame of an eigenvalue analysis.

A different situation is encountered on turning to one of the experiments in which the instability is not fully explained by modal analysis. Figures 16 and 17 report the results of the energy analysis conducted by considering the experimental conditions of experiment 6 of CGH, whose characteristics have already been commented on in

https://doi.org/10.1017/jfm.2014.155 Published online by Cambridge University Press

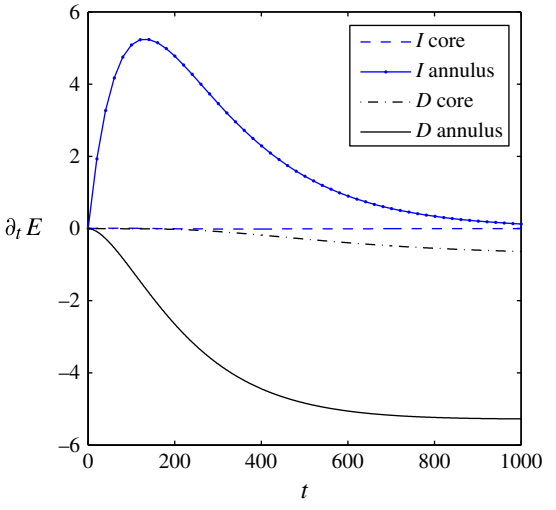


FIGURE 18. (Colour online) Decomposition of I and D into core and annulus components. The energy evolution is referred to the optimal perturbation with $n = 1$ and $k = 0$ for the parameters of experiment 6 of CGH.

previous sections. In figure 16 the time evolutions of the kinetic and potential energy components are displayed for two disturbances. The first one is the maximum growth rate unstable disturbance occurring at $n = 0$ and $k = 0.2266$ (figure 16*a*). The second is the $n = 1$, $k = 0$ disturbance, for which the maximum value of energy amplification occurs (figure 16*b*). The transient growth functions for these two disturbances have been presented in figure 6(*a*). The time evolutions of the energy components are obtained, as in the previous case, by considering optimal perturbations as initial conditions. Figure 16(*a*) shows that at early times unstable axisymmetric disturbances are weakly influenced by non-normality, while they develop mainly exponentially at moderate and high times, with a growth rate that is smaller than in the case previously considered. The analysis of the energy components reveals that in this case capillarity has little effect on the instability, since the term $(E_T - E_r)$ assumes small values. Figure 16(*b*), showing the evolution of the energy components for the spiral disturbance, provides evidence that the high levels of energy attained by this kind of perturbation are almost exclusively confined in the annular phase.

The energy budget for these two disturbances is reported in figure 17. Figure 17(*a*) confirms that capillarity does not influence the evolution of the perturbation, while most of the production of energy is due to the Reynold stress mechanism. The interfacial friction term B is almost negligible. Figure 17(*b*) shows that the energy amplification for (stable) spiral disturbances is governed by a more complex interplay between the various terms of the energy budget. At early times the Reynolds stress mechanism inputs energy into the system quite vigorously, while both dissipation and interfacial friction have little influence on the rate of change of the total kinetic energy. This effect, however, quickly saturates and at moderate and high times stability of the evolution is achieved by a balance between dissipation and interfacial friction. Note that in this plot the interfacial term $E_T - E_r$ is absent, since the disturbance evolves by keeping the surface of separation between the two phases constant.

The contribution to the total values of I and D by core and annular components is illustrated in figure 18. Once again, the extraction of energy from the base flow is

https://doi.org/10.1017/jfm.2014.155 Published online by Cambridge University Press

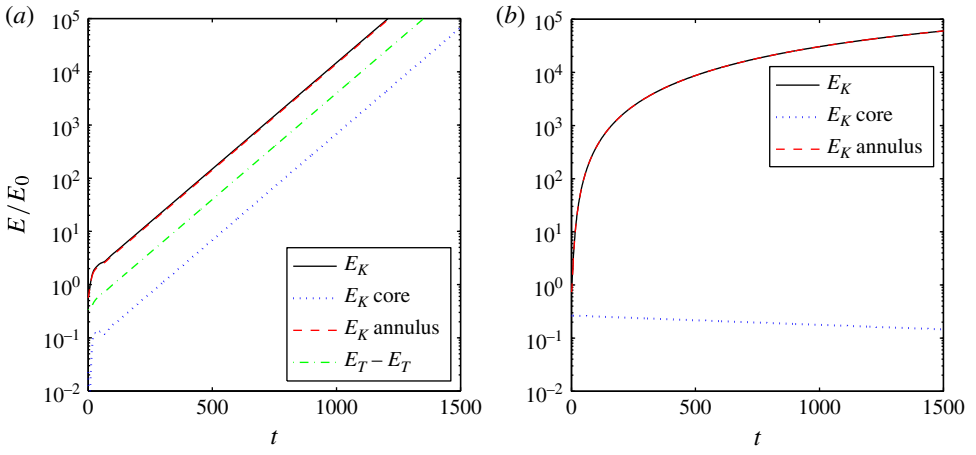


FIGURE 19. (Colour online) Time evolution of the kinetic and potential energy components for optimal perturbations relative to the parameters of the experiment illustrated in figure 6(*a*) of Sotgia *et al.* (2008): (*a*) $n = 0$ and $k = 2.3196$; (*b*) $n = 1$ and $k = 0$.

active only in the bulk of the annular phase, while dissipation occurs prevalently in the annular phase and only marginally in the core.

As a further example, let us consider the experiment represented in figure 6(*a*) of Sotgia *et al.* (2008) and already commented on in § 3.2. This is again a case in which the flow evolves toward a dispersed regime, with the oil core breaking and producing emulsions and drops in the water phase. This case differs from the previously considered one mainly because the viscosity ratio is much smaller (one order of magnitude smaller) and the annulus Reynolds number is higher. The time evolutions of the kinetic and potential energy components for this case are represented in figure 19. The disturbances considered are the ones whose growth functions are reported in figure 14(*a*), i.e. the axisymmetric fastest growing and $n = 1$, $k = 0$ perturbations. Figure 14 basically confirms the considerations for the previous case, the only visible differences being that for the axisymmetric disturbance the surface energy term has a remarkable stabilizing effect and that almost all the energy of the system is confined in the annulus.

The evolution of the components of the energy budget, reported in figure 20, shows that the interfacial friction term for the axisymmetric disturbance, (figure 20*a*), now has a noticeable role in producing energy, which at early times is mainly dissipated. The difference with respect to the previous case, in which the contribution of B to the energy budget was very weak, can be attributed to the presence of a stronger viscosity difference.

The effects of non-normality on spiral disturbances, on the oter hand, seem not to be influenced by the viscosity ratio, since the evolution in time of the various components of the energy budget (figure 20*b*) strongly resembles the analogous plot in figure 17, for the case of experiment 6 of CGH.

4. Conclusions

The classical problem of the stability of CAF has here been reconsidered from the point of view of linear non-modal analysis. The values of the governing parameters

https://doi.org/10.1017/jfm.2014.155 Published online by Cambridge University Press

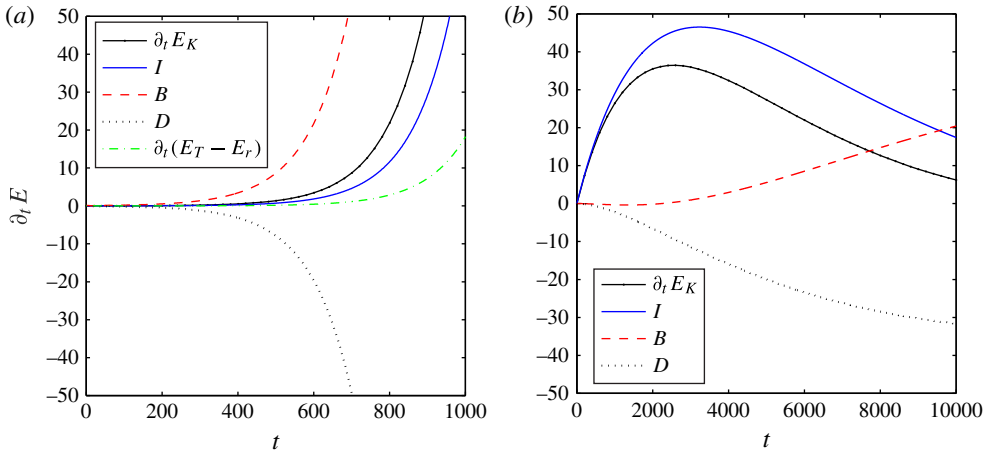


FIGURE 20. (Colour online) Evolution of the energy production and dissipation terms of the Reynolds–Orr equation for optimal perturbations relative to the parameters of the experiment illustrated in figure 6(*a*) of Sotgia *et al.* (2008): (*a*) $n = 0$ and $k = 2.3196$; (*b*) $n = 1$ and $k = 0$.

employed in the present investigation have been chosen in order to match the conditions of some classical experiments, for which quite a complete modal analysis was conducted in the past, and of more recent ones. For many of these experiments the presence of axisymmetric unstable modes (which are always the most unstable ones) at long waves can be successfully related to the occurrence of slugs or bubbles in the observed flow configurations. However, in some other circumstances these unstable modes are unable to explain what is physically observed, i.e. that the instability develops with irregular entrainment of water in the core region or of oil in the annular region. Moreover, the modal analysis reveals that the growth rates are usually quite low.

The present analysis of the non-normal features of the linear governing operator shows that in situations in which there is poor agreement between modal analysis and experimental results, there are disturbances that are affected by strong non-modal growth of energy. These disturbances have a spiral structure and long axial wavelength. The effects of the coexistence of exponentially unstable and stable but transiently growing disturbances have been studied by comparing the energy evolution of each disturbance family.

The analysis shows that for several decades of the non-dimensional time scale the energy levels of the stable disturbances are remarkably greater than those of the unstable ones. This allows us to argue that the irregular pattern observed in the experiments has its origin in the fast growth of spiral disturbances, which are able to promote the transition in the water well before the axisymmetric exponential instability prevails. The energy analysis of the system and the visualization of the pseudospectra confirm that most of the disturbance structure attaining the highest levels of energy is located in the annular less viscous phase.

Acknowledgement

This work has been developed within the F.A.R.O. project, funded by Polo delle Scienze e delle Tecnologie of Università degli Studi di Napoli ‘Federico II’.

https://doi.org/10.1017/jfm.2014.155 Published online by Cambridge University Press

Appendix A. Matrix components of the generalized eigenvalue problem (2.4)

In the original four-equation version, the non-null components of the operators $\mathscr{M}$ and $\mathscr{A}$ of (2.4) expressed in matrix form for the core phase are

$$\mathscr{M}_{11} = \mathscr{M}_{22} = \mathscr{M}_{33} = 1 \tag{A 1}$$

$$\left.\begin{aligned}
\mathscr{A}_{11} = \mathscr{A}_{22} &= -\mathrm{i}k\overline{W} + \frac{1}{Re_1}\left(\left[\partial_r^*\partial_r - \left(\frac{n^2}{r^2} + k^2\right)\right] - \frac{1}{r^2}\right) \\
\mathscr{A}_{12} = \mathscr{A}_{21} &= -\frac{1}{Re_1}\frac{2n}{r^2} \\
\mathscr{A}_{14} &= \mathrm{i}\partial_r \\
\mathscr{A}_{24} = \mathscr{A}_{42} &= -\mathrm{i}\frac{n}{r} \\
\mathscr{A}_{31} &= -\mathrm{i}\overline{W}' \\
\mathscr{A}_{33} &= -\mathrm{i}k\overline{W} + \frac{1}{Re_1}\left[\partial_r^*\partial_r - \left(\frac{n^2}{r^2} + k^2\right)\right] \\
\mathscr{A}_{34} = \mathscr{A}_{43} &= -\mathrm{i}k \\
\mathscr{A}_{41} &= -\mathrm{i}\partial_r^*
\end{aligned}\right\} \tag{A 2}$$

where the ordering of the variables is $(\tilde{u}, \tilde{v}, \tilde{w}, \tilde{p})$. Here, ∂_r stands for the derivative with respect to r, ∂_r^* is the *polar* derivative, $\partial_r^* = \partial_r + r^{-1}$. Analogous expressions are valid for the annular phase.

In the three-equation version, obtained by eliminating the pressure, the expressions are

$$\left.\begin{aligned}
\mathscr{M}_{11} = \mathscr{M}_{22} &= 1 \\
\mathscr{M}_{13} &= \frac{1}{k}\partial_r \\
\mathscr{M}_{23} &= -\frac{n}{rk}
\end{aligned}\right\} \tag{A 3}$$

$$\left.\begin{aligned}
\mathscr{A}_{11} &= -\mathrm{i}\left[k\overline{W} + \frac{1}{k}\left(\overline{W}'' + \overline{W}'\partial_r\right)\right] + \frac{1}{Re_1}\left\{\left[\partial_r^*\partial_r - \left(\frac{n^2}{r^2} + k^2\right)\right] - \frac{1}{r^2}\right\} \\
\mathscr{A}_{12} &= -\frac{1}{Re_1}\frac{2n}{r^2} \\
\mathscr{A}_{13} &= -\mathrm{i}\left(\overline{W}' + \overline{W}\partial_r\right) + \frac{1}{Re_1}\frac{1}{k}\left\{\partial_r\left[\partial_r^*\partial_r - \left(\frac{n^2}{r^2} + k^2\right)\right]\right\} \\
\mathscr{A}_{21} &= \mathrm{i}\frac{n}{rk}\overline{W}' - \frac{1}{Re_1}\frac{2n}{r^2} \\
\mathscr{A}_{22} &= -\mathrm{i}k\overline{W} + \frac{1}{Re_1}\left\{\left[\partial_r^*\partial_r - \left(\frac{n^2}{r^2} + k^2\right)\right] - \frac{1}{r^2}\right\} \\
\mathscr{A}_{23} &= \mathrm{i}\frac{n}{r}\overline{W} - \frac{1}{Re_1}\frac{n}{rk}\left[\partial_r^*\partial_r - \left(\frac{n^2}{r^2} + k^2\right)\right] \\
\mathscr{A}_{31} &= \partial_r^* \\
\mathscr{A}_{32} &= \frac{n}{r} \\
\mathscr{A}_{33} &= k.
\end{aligned}\right\} \tag{A 4}$$

https://doi.org/10.1017/jfm.2014.155 Published online by Cambridge University Press

The interface conditions at $r=1$ are

$$\left.\begin{gathered}\langle\tilde{u}\rangle=\langle\tilde{v}\rangle=0\\ \langle\tilde{w}\rangle+\left\langle\overline{W}'\right\rangle\tilde{\delta}=0\\ \tilde{u}-(k\overline{W}-\omega)\tilde{\delta}=0\\ \left\langle\frac{\zeta}{Re}\left(\partial_r\tilde{w}-k\tilde{u}\right)\right\rangle=0\\ \left\langle\frac{\zeta}{Re}\left(\partial_r\tilde{v}-\tilde{v}-n\tilde{u}\right)\right\rangle=0\\ -\langle\zeta\tilde{p}\rangle+2\mathrm{i}\left\langle\frac{\zeta}{Re}\partial_r\tilde{u}\right\rangle=\frac{J}{Re_1^2}\left(1-n^2-k^2\right)\tilde{\delta}.\end{gathered}\right\} \tag{A 5}$$

Note that $\langle\zeta\rangle$ has to be interpreted as $\zeta_1-\zeta_2=1-\zeta$.

The regularity conditions at the pipe axis ($r=0$) are dependent on the azimuthal wavenumber n,

$$\left.\begin{gathered}\tilde{u}=\tilde{v}=\partial_r\tilde{w}=\partial_r\tilde{p}=0,\quad \text{if } n=0,\\ \tilde{u}+n\tilde{v}=\partial_r\tilde{u}=\tilde{w}=\tilde{p}=0,\quad \text{if } |n|=1,\\ \tilde{u}=\tilde{v}=\tilde{w}=\tilde{p}=0,\quad \text{if } |n|>1.\end{gathered}\right\} \tag{A 6}$$

REFERENCES

Ash, R. L. & Khorrami, M. R. 1995 Vortex stability. In *Fluid Vortices,*, pp. 317–372. Kluwer.

Charles, M. E., Govier, G. W. & Hodgson, G. W. 1961 The horizontal pipeline flow of equal density oil–water mixtures. *Can. J. Chem. Engng* **39**, 17–36.

Charles, M. E. & Redberger, P. J. 1962 The reduction of pressure gradients in oil pipelines by the addition of water: numerical analysis of stratified flow. *Can. J. Chem. Engng* **40** (2), 70–75.

Chen, K. & Joseph, D. D. 1991 Lubricated pipelining: stability of core–annular flow. Part 4. Ginzburg–Landau equations. *J. Fluid Mech.* **227**, 226–260.

Coppola, G., Orazzo, A. & de Luca, L. 2012 Non-modal instability of core–annular flow. *Int. J. Nonlinear Sci. Numer. Simul.* **13**, 405–415.

Coppola, G. & Semeraro, O. 2011 Interfacial instability of two rotating viscous immiscible fluids in a cylinder. *Phys. Fluids* **23**, 064105.

Hickox, C. E. 1971 Instability due to viscosity and density stratification in axisymmetric pipe flow. *Phys. Fluids* **14**, 251–262.

Hu, H. H. & Joseph, D. D. 1989 Lubricated pipelining: stability of core–annular flow. Part 2. *J. Fluid Mech.* **205**, 359–396.

Joseph, D. D. & Renardy, Y. Y. 1991 *Fundamentals of Two-Fluid Dynamics*. Springer.

Joseph, D. D., Renardy, Y. & Renardy, M. 1985 Instability of the flow of immiscible liquids with different viscosities in a pipe. *J. Fluid Mech.* **141**, 309–317.

Khorrami, M. R., Malik, M. R. & Ash, R. L. 1989 Application of spectral collocation techniques to the stability of swirling flows. *J. Comput. Phys.* **81**, 206–229.

MacLean, D. L. 1973 A theoretical analysis of bicomponent flow and the problem of interface shape. *Trans. Soc. Rheol.* **17**, 385–399.

Malik, S. & Hooper, A. P. 2007 Three-dimensional disturbances in channel flows. *Phys. Fluids* **19**, 052102.

Miesen, R., Beijnon, G., Duijvestijn, P. E. M., Oliemans, R. V. A. & Verheggen, T. 1992 Interfacial waves in core–annular flow. *J. Fluid Mech.* **238**, 97–117.

https://doi.org/10.1017/jfm.2014.155 Published online by Cambridge University Press

OLIEMANS, R. V. A. & OOMS, G. 1986 Core–annular flow of oil and water through a pipeline. *Multiphase Sci. Technol.* **2**, 427–476.

PAPAGEORGIOU, D. T., MALDARELLI, C. & RUMSCHITZKI, D. S. 1990 Nonlinear interfacial stability of core–annular film flows. *Phys. Fluids* A **2** (3), 340–352.

PREZIOSI, L., CHEN, K. & JOSEPH, D. D. 1989 Lubricated pipelining: stability of core–annular flow. *J. Fluid Mech.* **201**, 323–356.

SCHMID, P. J. 2007 Non-modal stability theory. *Annu. Rev. Fluid Mech.* **39**, 129–162.

SCHMID, P. J. & HENNINGSON, D. S. 1994 Optimal energy density growth in Hagen–Poiseuille flow. *J. Fluid Mech.* **277**, 197–225.

SCHMID, P. J. & HENNINGSON, D. S. 2001 *Stability and Transition in Shear Flow*. Springer.

SOTGIA, G., TARTARINI, P. & STALIO, E. 2008 Experimental analysis of flow regimes and pressure drop reduction in oil–water mixtures. *Intl J. Multiphase Flow* **34**, 1161–1174.

TREFETHEN, L. N. & EMBREE, M. 2005 *Spectra and Pseudospectra: The Behavior of Nonnormal Matrices and Operators*. Princeton University Press.

TREFETHEN, L. N., TREFETHEN, A. E., REDDY, S. C. & DRISCOLL, T. A. 1993 Hydrodynamic stability without eigenvalues. *Science* **261**, 578–584.

https://doi.org/10.1017/jfm.2014.155 Published online by Cambridge University Press